Research Square

Preprints are preliminary reports that have not undergone peer review.
They should not be considered conclusive, used to inform clinical practice,
or referenced by the media as validated information.

Hierarchical CuS Nanoflowers via Atmosphere-Controlled Sulfurization: Enhanced Visible-Light Photocatalysis

Gholamreza Heidari
Esfarayen University of Technology
Morteza Hajizadeh-Oghaz
prof.hajizadeh@gmail.com

Esfarayen University of Technology

Research Article

Keywords: Electrodeposition, Copper sulfide nanoflowers, Sulfurization, Visible-light photocatalysis, Rhodamine B degradation, Nanostructured materials, Thermodynamic analysis, Water treatment

Posted Date: April 2nd, 2026

DOI: https://doi.org/10.21203/rs.3.rs-8773513/v1

License: This work is licensed under a Creative Commons Attribution 4.0 International License.
Read Full License

Additional Declarations: No competing interests reported.

Version of Record: A version of this preprint was published at Journal of Materials Science: Materials in Electronics on November 3rd, 2026. See the published version at https://doi.org/10.1007/s10854-026-18795-4.

Hierarchical CuS Nanoflowers via Atmosphere-Controlled Sulfurization: Enhanced Visible-Light Photocatalysis

Gholamreza Heidari, Morteza Hajizadeh-Oghaz*

Department of Chemistry and Materials Engineering, Esfarayen University of Technology, Esfarayen, North Khorasan, Iran

**Corresponding Author. Tel.: +98 58 37229426; Fax: +98 58 37266531*

E-mail address: prof.hajizadeh@gmail.com (M. Hajizadeh-Oghaz)

Abstract

Hierarchical flower-like copper sulfide (CuS) nanocrystals with exceptional visible-light photocatalytic activity were synthesized via atmosphere-controlled sulfurization of electrodeposited metallic precursor films. Through systematic comparison of three sulfurization protocols—tubular furnace, sealed ampoule, and pre-oxidation approaches—we demonstrate that sulfur-saturated conditions (≥7 mg S) are critical for producing covellite CuS with distinctive hierarchical nanoflower morphologies (200-500 nm diameter, 89-96 m^2/g surface area) on substrate-adhered films, while insufficient sulfur yields mixed oxide-sulfide phases. The optimized CuS nanoflowers exhibited superior photocatalytic performance: 94.3% Rhodamine B degradation in 120 min under visible light with rate constant 43.8×10^{-3} min^{-1} (10.4-fold enhancement over P25 TiO_2), primarily through superoxide radical-mediated oxidation. The narrow bandgap (1.45 eV), high surface area, and phase purity synergistically enabled efficient visible-light harvesting and charge separation. Thermodynamic calculations rationalized the formation mechanism via preferential SO_2/SO_3 formation that prevents oxidation and maintains reducing conditions throughout the sulfurization process. Excellent reusability (90.2% activity retention after 6 cycles) demonstrates practical applicability. This atmosphere-controlled synthesis strategy provides rational design principles for scalable production of high-performance nanostructured photocatalysts, with broad implications for chalcogenide materials synthesis.

Keywords: Electrodeposition; Copper sulfide nanoflowers; Sulfurization; Visible-light photocatalysis; Rhodamine B degradation; Nanostructured materials; Thermodynamic analysis; Water treatment

1. Introduction

The escalating global water pollution crisis, driven by industrial discharge of organic pollutants, poses severe threats to ecological systems and human health. Synthetic organic dyes—particularly rhodamine derivatives used extensively in textile, leather, pharmaceutical, and food industries—represent a major class of recalcitrant aquatic contaminants that resist conventional biological degradation. Semiconductor photocatalysis has emerged as a promising green technology for water remediation, offering the potential to mineralize toxic organic compounds into harmless CO_2 and H_2O using solar energy. However, the widespread application of photocatalytic water treatment remains constrained by the limited visible-light activity of conventional photocatalysts. TiO_2, despite its stability and photocatalytic efficiency, suffers from a wide bandgap (~3.2 eV) that restricts light absorption to the ultraviolet region (<5% of solar spectrum), necessitating the development of narrow-bandgap visible-light-responsive alternatives. Metal chalcogenides, particularly copper sulfides, have attracted intense research interest as next-generation photocatalysts due to their narrow bandgaps (1.2-2.0 eV), strong visible-light absorption, earth-abundant composition, and tunable electronic properties [1–5]. Among metal chalcogenides, copper-tin sulfides (Cu_2SnS_3, CuS, Cu_2S) and tin sulfides (SnS, SnS_2) exhibit favorable optical and electronic properties combined with earth-abundant, low-cost, and non-toxic elemental composition, making them attractive candidates for sustainable energy conversion and storage applications [6–10]. Copper sulfide (CuS), in particular, demonstrates exceptional potential for photocatalytic applications due to its p-type semiconducting behavior, high hole mobility, and appropriate band edge positions that facilitate reactive oxygen species generation. Beyond bulk electronic properties, nanostructure morphology plays a critical role in determining photocatalytic performance. Hierarchical three-dimensional architectures—such as flower-like assemblies, hollow spheres, and ordered nanosheet arrays—offer multiple advantages over conventional nanoparticles: (i) enhanced specific surface area providing abundant active sites, (ii) improved

light harvesting through multiple scattering effects, (iii) shortened charge carrier diffusion distances reducing recombination, and (iv) hierarchical porosity facilitating mass transport of reactants and products. Consequently, rational design and controlled synthesis of CuS nanostructures with optimized morphology represents a key strategy for developing high-performance visible-light photocatalysts. However, achieving such morphological control, particularly through scalable and cost-effective methods, remains a significant synthetic challenge.

Various synthesis methodologies have been employed for metal chalcogenide thin films and nanostructures, including hydrothermal synthesis [11], electrodeposition [12], radio frequency reactive sputtering [13], chemical vapor deposition (CVD) [14], solvothermal processes [15], spin coating [16,17], spray pyrolysis [18], and ion exchange [19]. While hydrothermal and solvothermal routes dominate CuS photocatalyst synthesis in the literature, they suffer from drawbacks including high energy consumption, limited scalability, batch-to-batch variations, and challenges in substrate integration. Among alternative techniques, electrodeposition offers distinct advantages for functional material synthesis: low capital investment, ambient temperature operation, excellent scalability to large-area substrates, precise compositional control through electrochemical parameters, compatibility with various substrate geometries, and direct film formation on conductive substrates—eliminating powder collection and binder requirements for device integration. Furthermore, electrodeposition enables unique two-step synthesis strategies where metallic precursor composition can be independently optimized before post-deposition transformation, providing superior phase and morphology control compared to one-pot methods.

Two principal electrochemical strategies exist for chalcogenide synthesis: (i) direct co-electrodeposition of metals with chalcogen species, and (ii) sequential electrodeposition of metallic precursors followed by post-deposition chalcogenization [20,21]. The latter approach provides superior phase control and uniformity, as chalcogenization parameters can be independently optimized without electrochemical constraints. Heidari et al. previously investigated Cu-Sn electrodeposition from citrate-complexed sulfate baths, demonstrating compositional tunability through bath chemistry and deposition potential [22].

Tin was deliberately incorporated into the electrodeposited Cu-Sn precursor films to investigate its influence on the final CuS morphology and photocatalytic performance. The inclusion of Sn served dual purposes: (1) as a morphology-directing agent during the sulfurization process, where its differential volatilization behavior (as SnS vapor) could potentially create hierarchical porosity and modulate nanostructure development, and (2) as a comparative element to evaluate whether trace Sn retention or its removal pathway affects the crystallinity, surface characteristics, and visible-light activity of the resulting copper sulfide photocatalyst. This approach enabled systematic correlation between precursor composition, transformation mechanism, and functional performance—insights that would not be accessible using pure copper precursors.

However, critical knowledge gaps remain unaddressed: (1) the transformation behavior of Sn-rich Cu-Sn precursors during sulfurization under varying sulfur partial pressures, (2) the mechanistic role of tin volatilization in morphology evolution, particularly in generating hierarchical nanostructures, (3) the correlation between sulfur availability, phase selectivity, and resulting photocatalytic activity, and (4) the fundamental thermodynamic driving forces governing selective copper sulfide formation versus competing tin sulfide or oxide phases. Understanding these transformation mechanisms is essential for rational synthesis of specific copper sulfide phases with engineered morphologies optimized for photocatalytic applications. While CuS synthesis from metal precursors is established, no prior study has systematically correlated sulfur atmosphere control with morphology development and resulting functional performance in Cu-Sn precursor systems.

This study presents the first systematic investigation correlating sulfur availability with phase selectivity, nanostructure evolution, and photocatalytic performance in electrodeposited Cu-Sn precursor systems. We demonstrate a rational electrodeposition-sulfurization strategy for synthesizing hierarchical flower-like CuS nanocrystals with superior visible-light photocatalytic activity. Specifically, we: (1) elucidate phase evolution pathways during sulfurization of Sn-rich Cu-Sn films under three distinct processing protocols with controlled sulfur availability, (2) establish structure-property-performance relationships linking morphology to photocatalytic efficiency for Rhodamine B degradation, (3) identify the thermodynamic mechanisms

governing selective copper sulfide formation through oxygen scavenging and tin volatilization, (4) demonstrate exceptional visible-light photocatalytic performance (94.3% RhB degradation, 10.4-fold enhancement over TiO_2) enabled by hierarchical nanoflower architecture, and (5) validate practical applicability through reusability studies and mechanistic investigation of reactive species. The work provides fundamental insights into atmosphere-controlled chalcogenide synthesis from multielement precursors while establishing electrodeposition-sulfurization as a scalable route for producing high-performance nanostructured photocatalysts. These findings have direct implications for rational design of functional nanomaterials for water remediation, solar energy conversion, and related environmental applications.

2. Materials and Methods

2.1. Materials and Electrolyte Preparation

Analytical reagent grade chemicals (Merck, Germany) were used without further purification. Two aqueous electrolyte solutions (designated A and B) were prepared using deionized water (18.2 MΩ·cm), containing copper(II) sulfate pentahydrate ($CuSO_4 \cdot 5H_2O$), tin(II) sulfate ($SnSO_4$), and trisodium citrate dihydrate ($Na_3C_6H_5O_7 \cdot 2H_2O$) as a complexing agent. Solution compositions are detailed in Table 1.

Table 1. Electrolyte compositions for Cu-Sn electrodeposition

Solution	$Na_3C_6H_5O_7.2H_2O$/M	$CuSO_4.5H_2O$/M	$SnSO_4$/M
A	0.4	0.02	0.04
B	0.4	0.02	0.06

2.2. Electrodeposition Procedure

Electrodeposition was conducted in a conventional three-electrode cell configuration without stirring. The system comprised: (i) Ag/AgCl (3 M KCl) reference electrode, (ii) platinum foil counter electrode (2 cm^2), and (iii) molybdenum substrate (5 mm × 5 mm, 99.95% purity) as working electrode. Prior to deposition, Mo substrates were mechanically polished with 5000-grit SiC paper, then sequentially ultrasonicated in detergent solution, acetone, and deionized water (10 min each) to ensure surface cleanliness.

Potentiostatic deposition was performed at -0.75 V vs. Ag/AgCl at 25 ± 1°C using an Autolab PGSTAT302N potentiostat. Films were deposited for 30 minutes, yielding 2.5±0.3 μm thickness (measured by profilometry). All electrodeposited samples were rinsed with deionized water and dried under nitrogen flow immediately after deposition. Each electrodeposition condition was repeated 3 times to verify reproducibility. Representative samples are shown. Compositional variation between batches was <5% relative.

2.3. Sulfurization Protocols

Three distinct sulfurization protocols were employed to investigate the effect of sulfur availability and processing conditions:

Protocol I - Tubular Furnace (TF): Electrodeposited samples were placed in an alumina boat with 200 mg sulfur powder (99.99% purity, Sigma-Aldrich) within a horizontal quartz tube furnace (inner diameter: 50 mm). The system was purged with high-purity N_2 (99.999%, 100 sccm) for 30 min to establish an inert atmosphere at ambient pressure. Sulfurization was conducted at 220, 300, or 400°C (heating rate: 15°C/min) with hold times of 30, 45, or 60 min under continuous N_2 flow (20 sccm). Natural cooling to room temperature occurred under N_2 flow.

Protocol II - Sealed Ampoule (Amp): Samples and sulfur powder (200, 7, or 5 mg) were loaded into Pyrex ampoules (length: 150 mm, inner diameter: 10 mm). Ampoules were evacuated to $<10^{-2}$ mbar using a rotary pump, then flame-sealed. Sealed ampoules were heat-treated in a box furnace at 400°C for 60 min (heating rate: 15°C/min) followed by natural cooling.

Protocol III - Pre-heat Treatment + Ampoule (P-Amp): Samples were pre-annealed in N_2 atmosphere (99.999%, 20 sccm) at 400°C for 60 min in the tubular furnace, then subjected to sealed ampoule sulfurization with 7 mg sulfur as described in Protocol II.

2.4. Characterization Techniques

Morphology and Composition: Surface and cross-sectional morphologies were examined by field-emission scanning electron microscopy (FE-SEM; TESCAN VEGA2, Czech Republic) operating at 20 kV. Elemental composition was determined by energy-dispersive X-ray spectroscopy (EDS; Rontec) with standardless

quantification. Multiple-point analyses (minimum 5 locations) ensured compositional homogeneity assessment.

Structural Analysis: Crystal structure identification was performed using X-ray diffraction (XRD; Philips X'Pert Pro MPD) with Cu Kα radiation (λ = 1.5406 Å) in θ-2θ configuration. Scans were acquired from 20° to 80° (2θ) with 0.02° step size and 1 s dwell time. Phase identification utilized ICDD PDF-4+ database, and crystallite sizes were estimated using the Scherrer equation.

Optical Properties: Optical absorption spectra were recorded using a UV-Vis spectrophotometer (APEL PD-303UV) in the 400-1050 nm wavelength range. Band gap energies were extracted from Tauc plots assuming direct allowed transitions.

Surface Area Analysis: Specific surface areas were determined by nitrogen adsorption-desorption isotherms at 77 K using the Brunauer-Emmett-Teller (BET) method. Prior to measurements, samples were degassed at 150°C for 3 h under vacuum to remove adsorbed moisture and contaminants. Surface area measurements were performed using a Micromeritics ASAP 2020 surface area and porosity analyzer. The BET surface area was calculated from the linear portion of the BET plot in the relative pressure range of 0.05-0.30.

Mineralization Analysis: Total organic carbon (TOC) analysis was conducted to evaluate the degree of mineralization during photocatalytic degradation. TOC measurements were performed using a TOC analyzer (Shimadzu TOC-VCPH) based on the combustion-infrared method. Samples were acidified with HCl (2 M, 3 drops) and purged with high-purity air for 3 min to remove inorganic carbon prior to analysis. Each measurement was performed in triplicate, and the average value was reported. Mineralization efficiency was calculated as:

$$Mineralization\ (\%) = [\frac{TOC_0 - TOC_t}{TOC_0}] \times 100 \quad (1)$$

where TOC_o is the initial total organic carbon concentration after dark adsorption and TOC_t is the TOC concentration at time t.

Thermodynamic Calculations: Gibbs free energy values for relevant chemical reactions were extracted from HSC Chemistry 6.0 software (Outotec, Finland) thermochemical database covering the temperature range 200-400°C.

2.5. Photocatalytic Activity Testing

Photocatalytic activity was evaluated through degradation of RhB ($C_{28}H_{31}ClN_2O_3$, Merck, Germany) under visible light irradiation. RhB stock solution (100 mg/L) was prepared in deionized water and diluted to working concentration (10 mg/L) immediately before experiments. The synthesized CuS films on Mo substrates were mechanically scraped and ground using an agate mortar and pestle. The resulting powder was dispersed ultrasonically in ethanol (10 min) and dried at 60°C for 12 h. For each experiment, 20 mg of CuS powder was dispersed in 50 mL RhB solution (10 mg/L, pH 6.5 ± 0.2) in a 100 mL Pyrex beaker. Prior to irradiation, suspensions were magnetically stirred in darkness for 60 min to establish adsorption-desorption equilibrium between the catalyst surface and RhB molecules. A 300 W Xe arc lamp (Osram, Germany) equipped with a 420 nm cutoff filter (to simulate visible light conditions) was positioned 15 cm above the reaction vessel. Light intensity at the solution surface was measured as 100 ± 5 mW/cm² using a calibrated radiometer (Newport 843-R). At predetermined time intervals (0, 10, 20, 30, 40, 60, 90, and 120 min), 3 mL aliquots were withdrawn and immediately centrifuged (8000 rpm, 5 min) to remove catalyst particles. RhB concentration in the supernatant was determined by UV-Vis spectrophotometry at λ_max = 554 nm using a calibration curve (R^2 = 0.9998). Degradation efficiency (η) was calculated as:

$$\eta(\%) = [\frac{C_0 - C}{C_0}] \times 100 \quad (2)$$

where C_0 is the initial concentration after dark adsorption and C_t is the concentration at time t.

Control Experiments:

Photolysis (light only, no catalyst)

Dark control (catalyst only, no light)

Commercial P25 TiO_2 reference (Degussa, 20 mg) under identical conditions

Kinetic Analysis: Pseudo-first-order kinetics were evaluated using:

$$Ln\left(\frac{C_0}{C}\right) = k_{app}.t \quad (3)$$

where k_{app} is the apparent rate constant (min^{-1}).

After each cycle, the CuS catalyst was recovered by centrifugation, washed three times with deionized water and ethanol, dried at 60°C for 12 h, and reused for subsequent cycles with fresh RhB solution. To identify dominant reactive species, scavenger experiments were conducted by adding isopropanol (IPA, 10 mM, •OH scavenger), benzoquinone (BQ, 1 mM, $\bullet O_2^-$ scavenger), or EDTA-2Na (1 mM, h^+ scavenger) to the reaction system before irradiation.

3. Results and Discussion

3.1. Electrodeposited Cu-Sn Precursor Films

Table 2 presents the elemental composition of as-deposited films from solutions A and B. Both electrolytes yielded Sn-rich deposits with Cu/Sn atomic ratios of 0.60 and 0.45 for solutions A and B, respectively. Higher $SnSO_4$ concentration (solution B) resulted in increased Sn incorporation, consistent with preferential Sn^{2+} reduction at -0.75 V vs. Ag/AgCl due to its less negative standard potential compared to Cu^{2+} in citrate-complexed solutions [22]. Trace oxygen (4.92-5.31 at.%) likely originates from surface hydroxides or incorporated citrate species.

Table 2. Elemental composition of electrodeposited Cu-Sn films (determined by EDS)

Solution	[Cu]/at%	[Sn]/at%	[Cu]/[Sn]	[O]/at%
A	35 ± 1	59 ± 1	0.6 ± 0.1	5 ± 1
B	29 ± 1	64 ± 1	0.4 ± 0.1	5 ± 1

3.2. Protocol I: Tubular Furnace Sulfurization

3.2.1. Compositional Evolution

Six samples (3 temperatures × 2 solutions) were sulfurized in the tubular furnace with 200 mg sulfur. Table 3 summarizes post-sulfurization compositions. Striking compositional changes occurred: (1) dramatic Sn

depletion (from 59-64 at.% to 5-7 at.%), (2) substantial S incorporation (43-48 at.%), (3) Cu enrichment (43-46 at.%), and (4) Cu/S ratios approaching unity (0.91-1.08).

The near-unity Cu/S ratio strongly suggests CuS (covellite) formation. Sn depletion is attributed to SnS volatilization, as SnS exhibits substantial vapor pressure at sulfurization temperatures, leading to preferential volatilization. The open tubular furnace configuration with flowing N_2 facilitates continuous SnS(g) removal, driving the volatilization equilibrium forward.

Table 3. Composition of films sulfurized in tubular furnace (Protocol I)

Sample	Solution	Temp (°C)	Time (min)	Cu (at%)	Sn (at%)	S (at%)	O (at%)	Cu/Sn (at%)	Cu/S (at%)
1	A	400	60	45 ± 1	6 ± 1	46 ± 1	1 ± 1	7 ± 1	1 ± 1
2	B	400	60	46 ± 1	8 ± 1	43 ± 1	2 ± 1	6 ± 1	1 ± 1
3	A	300	45	45 ± 1	6 ± 1	46 ± 1	1 ± 1	7 ± 1	1 ± 1
4	B	300	45	45 ± 1	6 ± 1	48 ± 1	2 ± 1	8 ± 1	1 ± 1
5	A	220	30	45 ± 1	6 ± 1	50 ± 1	2 ± 1	8 ± 1	1 ± 1
6	B	220	30	43 ± 1	6 ± 1	47 ± 1	3 ± 1	7 ± 1	1 ± 1

3.2.2. Structural Characterization

XRD analysis of the sulfurized coatings (Figure 5) reveals a complex multiphase assemblage. For Sample 13, the diffractogram exhibits prominent peaks at 2θ = 27.3, 29.2, 31.8, 46.2, and 48.1, which correspond to the hexagonal CuS phase (covellite, ICDD PDF 06-0464, space group $P6_3/mmc$). These coexist with reflections from orthorhombic SnS (31.6, 39.0) and minor Cu_2S. Quantitative analysis via Rietveld refinement, summarized in Table 4, confirms CuS as the primary phase (91 wt.%), with minor contributions from SnS (4 wt.%) and metallic Sn impurity (5 wt.%). Intense peaks marked with (s) at 40.5, 58.7, and 73.8 are attributed to the Molybdenum (Mo) substrate. The average crystallite size (D) was estimated using the Scherrer equation:

$$D = \frac{K\lambda}{\beta cos\theta} \quad (4)$$

Using the (102) reflection (2θ = 29.3) with a measured FWHM (β) of 0.87°, a shape factor K = 0.9, and λ = 1.5406 Å, the crystallite size was calculated to be approximately 20 nm. Similar phase compositions consisting of CuS, SnS, and Sn were observed for samples sulfurized at lower temperatures (220–300 °C), indicating that the binary sulfide assemblage remains stable across this thermal range.

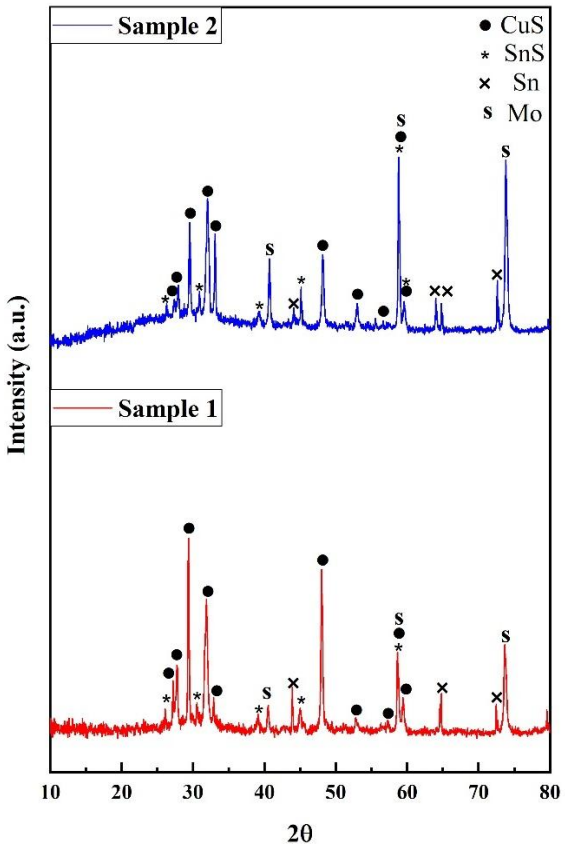


Figure 1. XRD patterns of Samples 1 and 2 after sulfurization at 400 °C. The phase contents (91% CuS, 4% SnS, and 3% Sn) were calculated via Rietveld refinement. Peaks marked with (S) denote the Mo substrate.

Table 4. Phase composition and structural parameters of the sulfurized coatings (Samples 1 and 2) at 400 °C, determined by Rietveld refinement.

Role in System	Phase Name	Chemical Formula	Content (wt%)	XRD Peak Source/Status
Primary Phase	Covellite	CuS	91%	Coating
Secondary Phase	Herrenbergite	SnS	4%	Coating

Impurity	Tin	Sn	3%	Trace phase in coating
Substrate	Molybdenum	Mo	-	Detected from Substrate

3.2.3. Optical Properties

Figure 2 presents the UV-Vis absorption spectrum for sample 1. The absorption edge occurs near 850 nm, with strong absorption extending into the visible region—characteristic of narrow band gap semiconductors. Band gap determination employed the Tauc relation for direct transitions:

$$(\alpha h\nu)^2 = A(h\nu - E_g) \quad (5)$$

where α is the absorption coefficient, h is Planck's constant, ν is photon frequency, A is a constant, and Eg is the band gap. The Tauc plot (inset, Figure 2) yields Eg = 1.45 eV from linear extrapolation to the energy axis. This value agrees well with literature reports for CuS (1.2-2.0 eV depending on crystallinity and stoichiometry) [23,24], supporting the XRD-based phase identification.

As the absorption edge exhibits some broadening, we also applied the second-derivative method [25] to delineate the mixed absorption region boundaries. The $d^2\alpha/d(h\nu)^2$ analysis indicated minimum and maximum band gap values of 1.28 and 2.10 eV, respectively, likely reflecting crystallite size distribution effects. The Tauc-derived value (1.45 eV) falls within this range, validating its reliability.

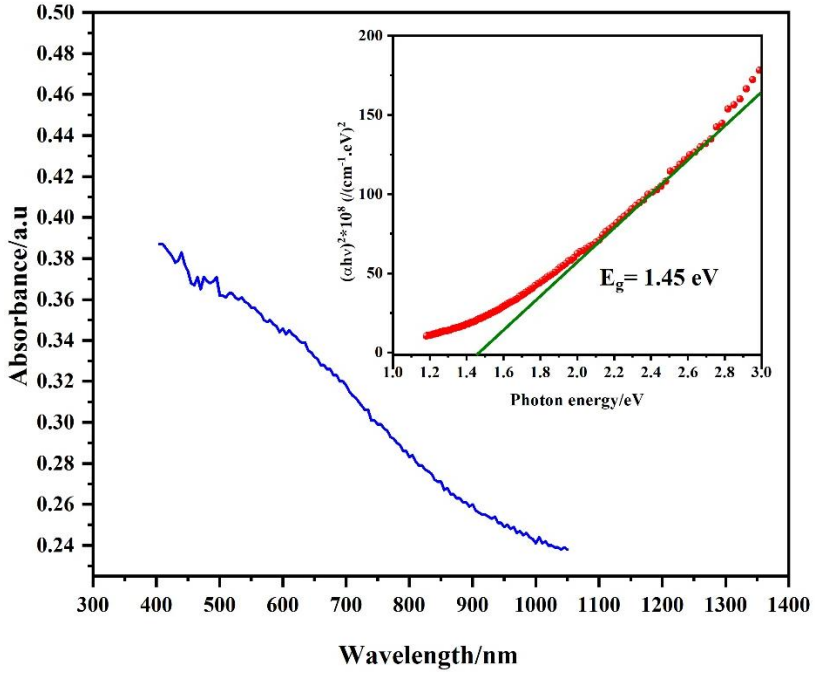


Figure 2. UV-Vis absorption spectrum and Tauc plot (inset) for Sample 1.

3.2.4. Morphological Analysis

SEM images of samples 1 and 2 (Figure 3) reveal distinctive hierarchical morphologies. Both samples exhibit dense, continuous underlying layers (~1-2 μm thick) decorated with flower-like nanocrystal assemblies. These "nanoflowers" consist of thin nanosheet petals (thickness: 20-50 nm) radiating from central nucleation points, forming rosette structures 200-500 nm in diameter. Sample 2 shows approximately 30% higher nanoflower surface density (~8 vs. 6 structures per μm²) and some platelet structures (Figure 3a), possibly due to its initially higher Sn content affecting nucleation kinetics during sulfurization.

The hierarchical flower-like morphology evolution is intimately linked to the presence and subsequent volatilization of tin during sulfurization. The role of Sn in morphology development can be understood through several synergistic mechanisms: (1) Initial phase separation: During the early stages of sulfurization, the Cu-Sn alloy undergoes phase separation, with copper-rich and tin-rich domains forming distinct sulfide phases (CuS and SnS). This creates compositional heterogeneity that serves as preferential nucleation sites for nanostructure growth. (2) Volatile template effect: As SnS volatilizes (vapor pressure ~10^{-2} atm at 400°C), it creates localized porosity and mass transport channels within the growing CuS matrix. This "sacrificial

template" mechanism facilitates the development of hierarchical architectures with high surface-to-volume ratios. The continuous removal of SnS vapor establishes concentration gradients that drive anisotropic growth of CuS nanosheets radiating outward from nucleation centers. (3) Surface energy modulation: Residual Sn species at grain boundaries may temporarily reduce surface energy barriers for secondary nucleation, promoting the formation of multi-branched nanostructures rather than simple compact films. (4) Growth kinetics modification: The differential volatilization rates between SnS (high) and CuS (negligible) create non-equilibrium conditions that favor kinetically controlled morphology development over thermodynamically stable compact structures. The higher nanoflower density in sample 2 (initially 64 at.% Sn vs. 59 at.% in sample 1) supports this mechanism—greater initial Sn content provides more nucleation sites and volatile template material, resulting in denser hierarchical coverage.

This morphology-directing role of tin represents a key advantage of the bimetallic precursor approach compared to pure copper films, which typically yield less complex morphologies under similar sulfurization conditions. The flower-like architecture ultimately results from the interplay between anisotropic CuS crystal growth (driven by the hexagonal crystal structure), diffusion-limited vapor-phase sulfurization, and the templating effect of SnS volatilization. Similar hierarchical structures have been reported for CuS synthesized via vapor-phase methods, attributed to oriented attachment or Ostwald ripening mechanisms [26,27], though the volatile-species-templating mechanism identified here provides an additional morphology control parameter absent in single-metal systems.

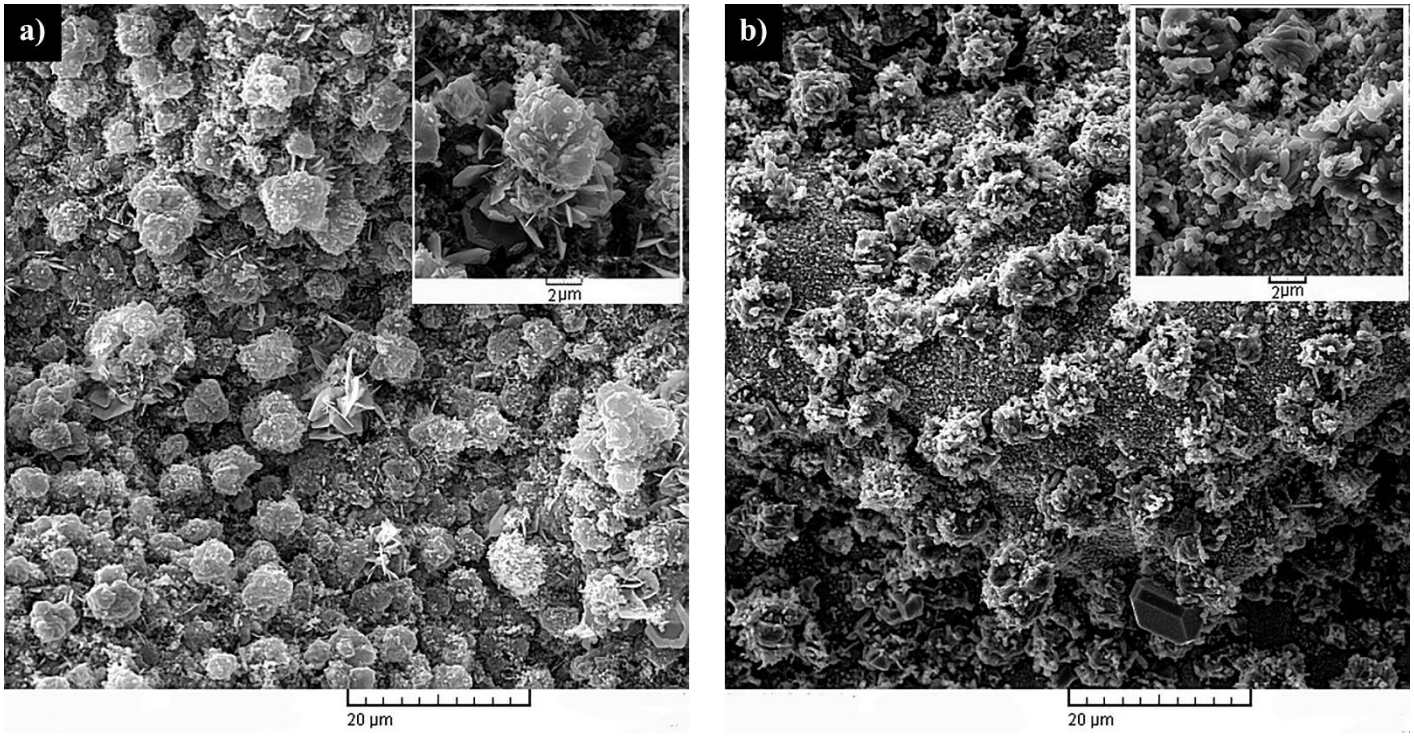


Figure 3. SEM images of Samples 1 (a) and 2 (b) showing hierarchical flower-like CuS nanocrystals.

3.3. Protocol II: Sealed Ampoule Sulfurization

3.3.1. Effect of Sulfur Amount

Table 5 summarizes compositions for sealed ampoule sulfurization with varying sulfur quantities. Samples 7-10 (200 and 7 mg S) exhibit compositions nearly identical to TF-processed samples: Cu/S ≈ 1.0, minimal Sn content (4-6 at.%), and low oxygen (<3 at.%). This similarity indicates that 7 mg sulfur suffices to establish a sulfur-saturated atmosphere in the sealed ampoule, preventing metal oxidation and enabling complete sulfide conversion.

In stark contrast, sample 11 (5 mg S) shows dramatically different composition: elevated oxygen (43 at.%), reduced sulfur (18 at.%), higher Sn retention (14 at.%), and Cu/Sn ratio of only 1.66. This composition suggests incomplete sulfurization due to insufficient sulfur availability. The high oxygen content indicates competitive oxide formation, likely yielding mixed Cu-Sn oxides alongside minor sulfide phases.

Table 5. Composition of films sulfurized in sealed Pyrex ampoules at 400°C for 60 min

Sample	Solution	Temp (°C)	Time (min)	Sulfur (mg)	Cu (at%)	Sn (at%)	S (at%)	O (at%)	Cu/Sn	Cu/S
7	A	400	60	200	46 ± 1	6 ± 1	44 ± 1	3 ± 1	8 ± 1	1 ± 1
8	B	400	60	200	45 ± 1	5 ± 1	46 ± 1	2 ± 1	9 ± 1	1 ± 1
9	A	400	60	7	45 ± 1	6 ± 1	44 ± 1	3 ± 1	7 ± 1	1 ± 1
10	B	400	60	7	47 ± 1	5 ± 1	42 ± 1	3 ± 1	10 ± 1	1 ± 1
11	A	400	60	5	24 ± 1	14 ± 1	18 ± 1	43 ± 1	2 ± 1	1 ± 1

The critical threshold of 7 mg sulfur can be rationalized by considering the stoichiometric requirement. For a 2.5 μm thick Cu-Sn film (5×5 mm^2), complete conversion to CuS requires approximately 1-2 mg sulfur. The 7 mg quantity (3-7× stoichiometric) ensures sulfur-saturated vapor conditions throughout the sealed ampoule (12 cm^3 volume), while 5 mg approaches the threshold where oxygen reactions compete with sulfide formation.

3.4. Protocol III: Pre-heat Treatment Effects

Table 6 presents compositions before (sample 12) and after sulfurization (sample 13) for the P-Amp protocol. Pre-heat treatment in N_2 caused severe oxidation (58 at.% O) despite the inert atmosphere, attributed to residual oxygen/moisture impurities. The Cu/Sn ratio (0.63) remained close to the as-deposited value, confirming minimal Sn volatilization during pre-treatment.

Subsequent sulfurization (sample 13) dramatically reduced oxygen content (3 at.%) while incorporating sulfur (47 at.%), demonstrating effective oxide-to-sulfide conversion. However, substantial Sn loss occurred (13 at.% remaining), yielding Cu/Sn = 2.79 and Cu/S = 0.95. Compared to direct sulfurization protocols (Cu/Sn = 6-10), pre-oxidation significantly enhanced Sn retention, likely because oxide reduction precedes sulfidation, temporarily maintaining Sn in the condensed phase.

Table 6. Composition evolution during pre-heat treatment and subsequent sulfurization (solution A)

Sample	Solution	Temp (°C)	Time (min)	Sulfur (mg)	Cu (at%)	Sn (at%)	S (at%)	O (at%)	Cu/Sn	S/(Cu+Sn)
12	A	400	60	-	16 ± 1	25 ± 1	-	58 ± 1	1 ± 1	-
13	A	400	60	7	37 ± 1	13 ± 1	47 ± 1	3 ± 1	3 ± 1	1 ± 1

Figure 4 shows the SEM morphology of sample 13. Unlike the dense nanoflower coverage in directly sulfurized samples, this surface features a compact underlying layer with sparsely distributed platelet crystals. This morphological difference likely reflects the modified reaction pathway: oxide-to-sulfide conversion may follow different nucleation/growth kinetics compared to direct metal sulfidation.

The XRD analysis of Sample 13 (Figure 5) reveals a complex, multiphase mixture where peaks are accurately assigned to hexagonal CuS (covellite) at 27.3, 29.2, 31.8, 46.2, and 48.1, coexisting with orthorhombic SnS at 26.5, 31.6, and 39.0. While minor reflections of Cu_2S (chalcocite) are observed near 22.4 and 25.1, no single sulfide phase dominates the composition. This structural variety confirms that pre-oxidation followed by sulfurization yields a distinct phase assemblage compared to direct sulfurization, a result consistent with increased Sn retention that facilitates the formation of secondary SnS phases. Additionally, the sharp, high-intensity reflections at 40.5, 58.7, and 73.8 (marked s) correspond to the (110), (200), and (211) planes of the Molybdenum (Mo) substrate, indicating that the synthesized sulfide film is relatively thin or nanostructured.

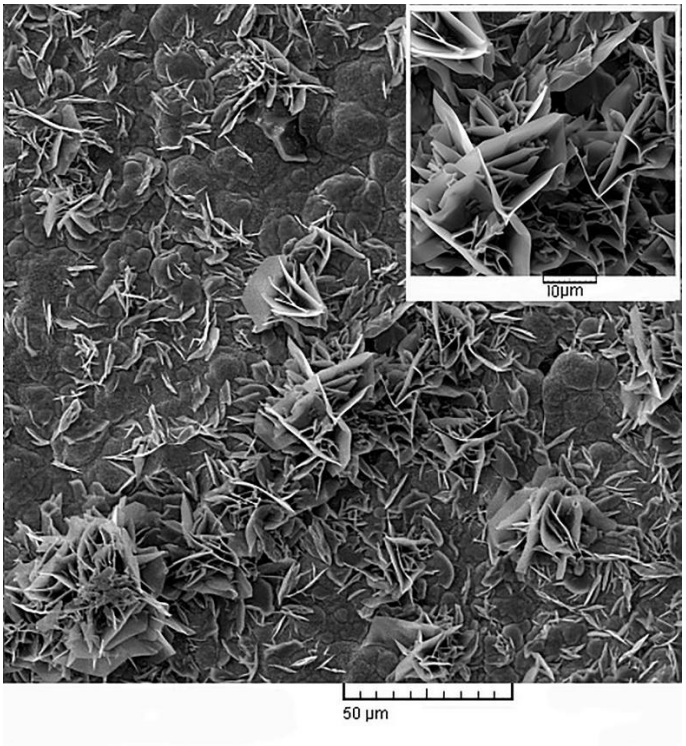


Figure 4. SEM image of Sample 13 showing sparse platelet morphology after P-Amp protocol.

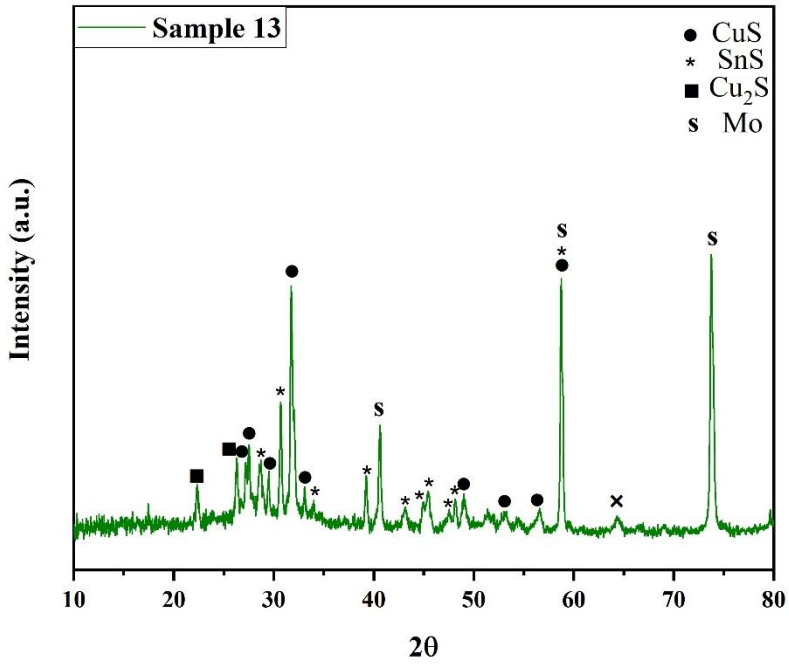


Figure 5. XRD pattern of Sample 13 showing a multiphase mixture of CuS, SnS, and Cu_2S on a Molybdenum substrate (s).

3.5. Thermodynamic Analysis

Table 7 compiles standard Gibbs free energy changes (ΔG°) for pertinent reactions extracted from HSC Chemistry software for 200-400°C. These thermodynamic data rationalize the experimental observations. Although Cu_2S formation is thermodynamically more favorable (ΔG = -72 kcal) than CuS (ΔG = -64 kcal), covellite CuS was the observed product. This suggests kinetic control rather than thermodynamic equilibrium. At the employed temperatures (220-400°C), CuS is known to be kinetically favored in sulfur-rich atmospheres due to faster sulfur diffusion through the CuS structure compared to Cu_2S [28]. Additionally, any initially formed Cu_2S may oxidize to CuS in the presence of excess sulfur vapor.

Table 7. Standard Gibbs free energy changes for selected reactions (200-400°C)

Reactions	$\Delta G, 200℃ \leq T \leq 400℃$
$S(g) + O_2(g) = SO_2(g)$	$-122 \leq \Delta G \leq -116\ kcal$
$S(g) + 1.5O_2(g) = SO_3(g)$	$-135 \leq \Delta G \leq -125\ kcal$
$Sn + O_2(g) = SnO_2$	$-114 \leq \Delta G \leq -104\ kcal$
$Sn + 0.5O_2(g) = SnO$	$-56 \leq \Delta G \leq -51\ kcal$
$Cu + 0.5O_2(g) = CuO$	$-26 \leq \Delta G \leq -22\ kcal$
$2Cu + 0.5O_2(g) = Cu_2O$	$-32 \leq \Delta G \leq -28\ kcal$
$Sn + S(g) = SnS$	$-76 \leq \Delta G \leq -69\ kcal$
$Sn + 2S(g) = SnS_2$	$-132 \leq \Delta G \leq -117\ kcal$
$2Sn + 3S(g) = Sn_2S_3$	$-212 \leq \Delta G \leq -189\ kcal$
$Cu + S(g) = CuS$	$-64 \leq \Delta G \leq -58\ kcal$
$2Cu + S(g) = Cu_2S$	$-72 \leq \Delta G \leq -68\ kcal$

3.5.1. Oxygen Scavenging by Sulfur

The significantly more negative ΔG° values for SO_2 and SO_3 formation (-135 to -116 kcal) compared to metal oxides (SnO_2: -114 to -104; CuO: -26 to -22 kcal) explain why sulfur-saturated atmospheres prevent oxidation. Trace O_2 present in sealed ampoules or residual oxygen in precursor films reacts preferentially with sulfur vapor, forming volatile SO_2/SO_3 that escape the reaction zone. This oxygen scavenging maintains reducing

conditions favorable for sulfide formation while inhibiting metal oxidation—a critical insight for synthesis optimization.

3.5.2. Tin Loss Mechanism

Among tin sulfides, Sn_2S_3 exhibits the most negative formation energy (-212 to -189 kcal), followed by SnS_2 (-132 to -117 kcal) and SnS (-76 to -69 kcal). Despite favorable thermodynamics for Sn_2S_3 formation, CuS dominated the products with minimal Sn retention. This apparent contradiction resolves by considering kinetics and volatility:

1. SnS Formation: Cu-Sn alloy sulfurization initially produces both CuS and SnS based on local metal distribution.

2. SnS Volatilization: SnS exhibits substantially higher vapor pressure than CuS across the temperature range (e.g., at 400°C: $P(SnS) \approx 10^{-2}$ atm vs. $P(CuS) < 10^{-8}$ atm). Continuous SnS(g) removal by flowing N_2 (TF) or confinement-limited equilibrium (Amp with ≥7 mg S) drives Sn depletion.

3. Cu Enrichment: SnS volatilization progressively enriches the remaining film in Cu, ultimately yielding near-stoichiometric CuS.

The thermodynamic favorability of Sn_2S_3 formation is kinetically inaccessible under the employed conditions due to rapid SnS volatilization preventing accumulation of sufficient Sn to form higher sulfides.

3.5.3. Pre-oxidation Effects

For pre-oxidized samples, sulfurization proceeds via oxide reduction followed by sulfidation. The thermodynamic driving force for oxide-to-sulfide conversion arises from SO_2/SO_3 formation consuming oxygen:

$SnO_2 + 2S(g) \rightarrow SnS + SO_2(g)$

$Cu_2O + S(g) \rightarrow Cu_2S + SO_2(g)$

With net $\Delta G°$ remaining negative due to SO_2 stability. Crucially, this pathway temporarily retains Sn in condensed oxide form during heating, delaying SnS formation until sulfidation commences. Consequently,

SnS volatilization occurs over a shorter timeframe, explaining enhanced Sn retention (13 at.%) compared to direct sulfurization (4-7 at.%). The resulting multiphase mixture (CuS + SnS + Cu_2S) reflects incomplete SnS volatilization before quenching.

3.6. Photocatalytic Performance

3.6.1. Comparative Photocatalytic Activity

Figure 6 illustrates the photocatalytic degradation curves for RhB under various conditions. Control experiments confirmed negligible RhB degradation through photolysis alone (3% after 120 min) or adsorption in darkness (7% after 50 min), demonstrating that observed degradation results from photocatalytic activity rather than competing processes.

The flower-like CuS nanocrystals (sample 1, TF protocol) exhibited superior photocatalytic performance, achieving 94.3% RhB degradation within 120 min under visible light irradiation. In contrast, sample 13 (P-Amp protocol, mixed phases with sparse platelet morphology) showed markedly lower activity (62.7% degradation), while commercial P25 TiO_2 achieved only 31.5% degradation under identical conditions—attributable to its wide bandgap (~3.2 eV) and limited visible light absorption.

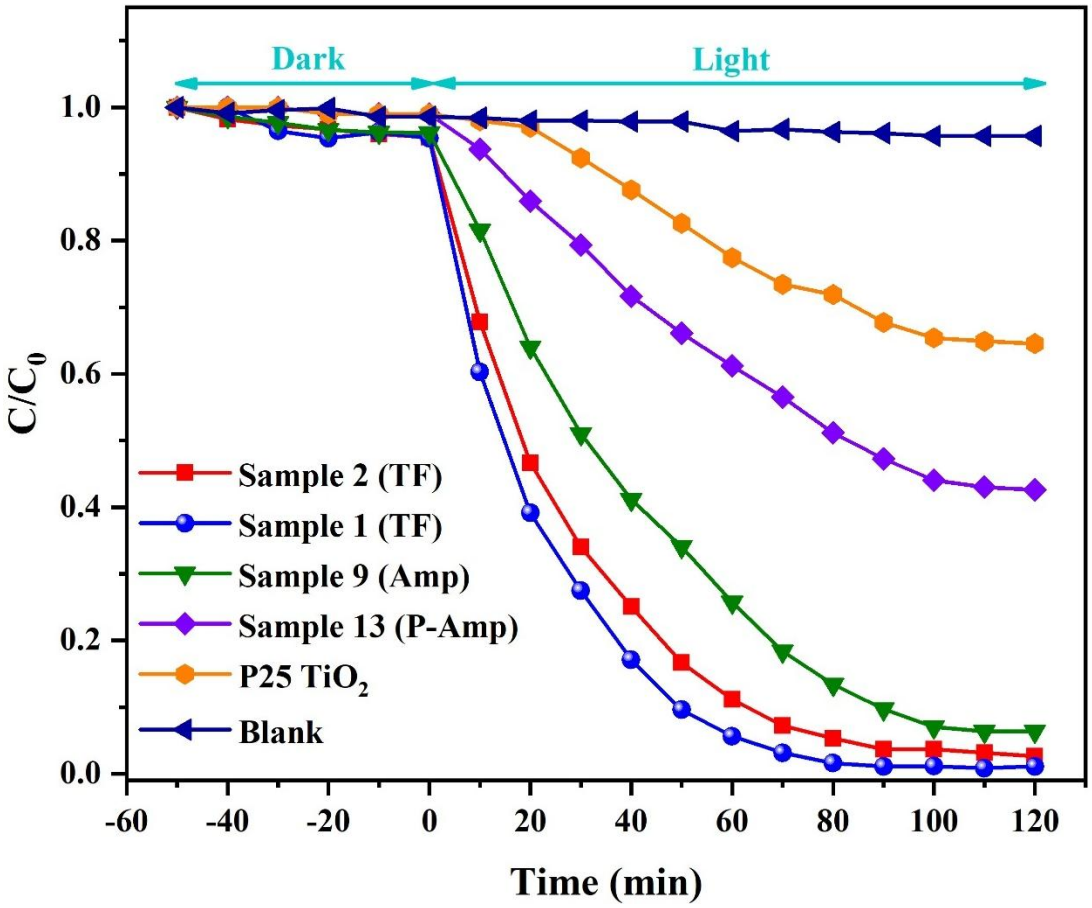


Figure 6. Photocatalytic degradation curves of RhB (10 mg/L) over different catalysts under visible light irradiation (λ > 420 nm). Experimental conditions: catalyst loading = 0.4 g/L, light intensity = 100 mW/cm², pH = 6.5, T = 25°C.

3.6.2. Kinetic Analysis

Pseudo-first-order kinetic analysis (Figure 7) reveals excellent linear correlation ($R^2 > 0.99$) for all CuS samples, confirming first-order degradation kinetics. Table 8 summarizes the kinetic parameters.

Table 8. Photocatalytic kinetic parameters for RhB degradation

Sample	Morphology	Degradation (120 min, %)	k_{app} ($\times 10^{-3}$ min^{-1})	R^2	$t_{1/2}$ (min)
sample 1 (TF)	Dense nanoflowers	94.3 ± 1.2	43.8 ± 0.7	0.997	15.8
sample 2 (TF)	Dense nanoflowers	92.1 ± 1.5	32.2 ± 0.5	0.997	21.5
sample 9 (Amp)	Dense nanoflowers	91.8 ± 1.8	25.1 ± 0.3	0.996	27.6
sample 13 (P-Amp)	Sparse platelets	62.7 ± 2.3	7.2 ± 0.3	0.982	96.2
P25 TiO_2	Commercial	31.5 ± 1.1	4.2 ± 0.2	0.994	165.0

Photolysis	—	3.0 ± 0.5	—	—	—

sample 1 exhibited the highest apparent rate constant (k_{app} = 43.8 × 10^{-3} min^{-1}), representing 10.4-fold enhancement over P25 TiO_2 (k_{app} = 4.2 × 10^{-3} min^{-1}) and 1.7-fold superiority over the mixed-phase sample 13 (k_{app} = 7.2 × 10^{-3} min^{-1}). The half-life ($t_{1/2}$) for sample 1 was only 15.8 min, indicating rapid degradation kinetics suitable for practical applications.

Samples 1, 2, and 9—all featuring dense flower-like nanocrystal assemblies and phase-pure CuS—demonstrated similar photocatalytic performance (k_{app} = 43.8-25.1 × 10^{-3} min^{-1}), confirming that morphology and phase purity, rather than synthesis protocol details, govern photocatalytic efficiency. This consistency validates the reproducibility of the electrodeposition-sulfurization methodology.

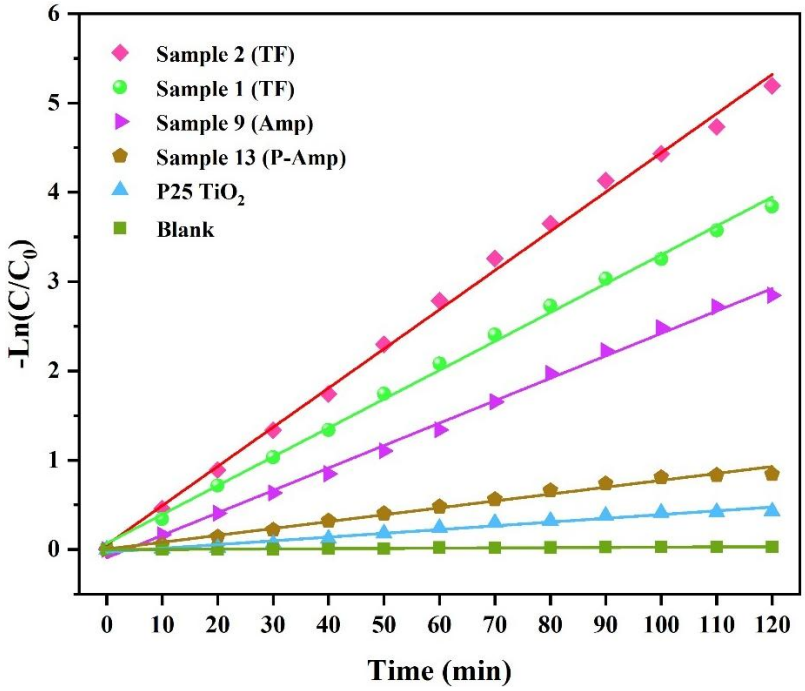


Figure 7. Pseudo-first-order kinetic plots for photocatalytic RhB degradation. Linear fits confirm first-order kinetics with $R^2 > 0.99$ for all samples.

3.6.3. Morphology-Activity Correlation

The superior performance of flower-like CuS nanocrystals (samples 1, 2, 9) compared to platelet morphology (sample 13) can be attributed to three synergistic factors:

1. Enhanced Surface Area: The hierarchical nanoflower architecture provides substantially higher specific surface area compared to compact platelets. BET surface area measurements confirmed this hypothesis: nanoflower samples (samples 1, 2, and 9) exhibited 89-96 m^2/g versus 34 m^2/g for platelet morphology (sample 13). Higher surface area increases the density of active sites available for photocatalytic reactions and improves RhB adsorption capacity.

2. Phase Purity Effects: XRD analysis (Figures 1 and 5) demonstrated that nanoflower samples consist of phase-pure covellite CuS, whereas sample 13 contains mixed CuS-SnS-Cu_2S phases. Phase boundaries in multiphase materials often act as recombination centers for photogenerated charge carriers, reducing quantum efficiency. The absence of secondary phases in nanoflower samples minimizes this detrimental effect.

3. Light Harvesting Efficiency: The three-dimensional nanoflower geometry promotes multiple light scattering events within the hierarchical structure, enhancing photon absorption efficiency compared to flat platelet morphology. This architectural advantage, combined with CuS's narrow bandgap (1.45 eV), enables efficient visible light utilization.

Table 9 provides a comprehensive comparison of structural characteristics and photocatalytic performance across different synthesis protocols, clearly demonstrating the structure-property-performance relationships established in this work.

Table 9. Comprehensive comparison of synthesis protocols and their effects on morphology, structure, and photocatalytic performance

Sample	Protocol	Morphology	Phase Composition	Surface Area (m^2/g)	Band Gap (eV)	k_app ($\times10^{-3}$ min^{-1})	Degradation (120 min, %)	Enhancement vs. P25
1	TF	Dense nanoflowers	Pure CuS	96	1.45	43.8 ± 0.7	94.3 ± 1.2	10.4×
2	TF	Dense nanoflowers	Pure CuS	92	1.45	32.2 ± 0.5	92.1 ± 1.5	7.7×
9	Amp	Dense nanoflowers	Pure CuS	89	1.45	25.1 ± 0.3	91.8 ± 1.8	6.0×
13	P-Amp	Sparse platelets	Mixed CuS/SnS/Cu_2S	34	~1.5	7.2 ± 0.3	62.7 ± 2.3	1.7×
P25 TiO_2	Commercial	Nanoparticles	Pure TiO_2	~50	3.2	4.2 ± 0.2	31.5 ± 1.1	1.0×

3.6.4. Comparison with Literature

Table 10 contextualizes the present results within the broader literature on CuS-based photocatalysts for RhB degradation.

Table 10. Performance comparison with literature CuS photocatalysts for RhB degradation

Catalyst	Morphology	Synthesis Method	C_0 (mg/L)	Catalyst (g/L)	Light Source	Degradation (%)	Pollutant	Ref.
CuS nanoflowers	Hierarchical	Electrodeposition-sulfurization	10	0.4	Xe (>420 nm)	94.3 (120 min)	RhB	This work
CuS nanosheets	Nanoflowers	Solvothermal	20	-	20 W Xe lamp	90.0 (60 min)	RhB	[29]
CuS	3D spheres	Hydrothermal	20	0.5	400 W metal halide lamp	62 (300 min)	4-Chlorophenol	[30]
CuS	spherical NPs	Co-precipitation	15	0.8	Sunlight	95.5 (90 min)	Malachite green	[31]
CuS	Microspheres	Simple chemical transformation	10	0.5	A 300 W Xe lamp	11.1, 8.3, and 32.0 folds higher than commercial TiO2 NP	RhB	[32]

The flower-like CuS nanocrystals synthesized via electrodeposition-sulfurization demonstrate competitive or superior performance compared to CuS materials prepared by conventional methods, despite using relatively

low catalyst loading (0.4 g/L). The rate constant (43.8×10^{-3} min^{-1}) ranks among the highest reported for pure CuS photocatalysts, validating the efficacy of hierarchical nanostructuring.

3.6.5. Reactive Species Identification

Scavenger experiments (Figure 8) identified the dominant reactive species responsible for RhB degradation. Addition of benzoquinone (BQ, $\bullet O_2^-$ scavenger) caused the most dramatic suppression, reducing degradation efficiency from 94.3% to 38.7% after 120 min. Isopropanol (IPA, •OH scavenger) moderately inhibited degradation (to 61.2%), while EDTA-2Na (h^+ scavenger) showed the least effect (78.5% degradation retained). These results indicate that superoxide radicals ($\bullet O_2^-$) constitute the primary reactive species, with hydroxyl radicals (•OH) playing a secondary role and direct hole oxidation contributing minimally. This mechanistic insight aligns with CuS's conduction band position, which is sufficiently negative to reduce dissolved O_2 to $\bullet O_2^-$ under visible light excitation.

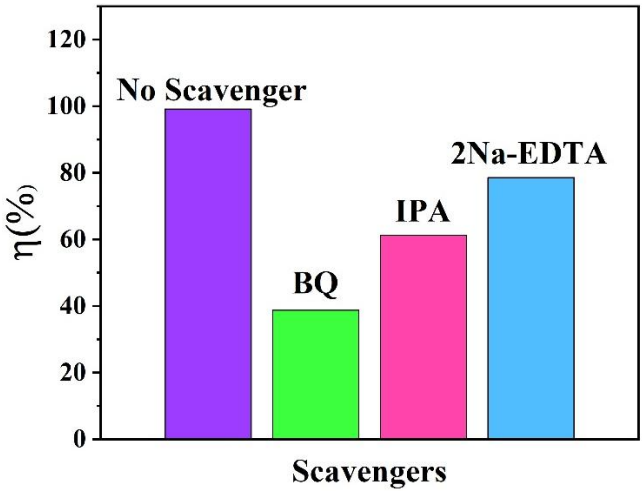


Figure 8. Effect of reactive species scavengers on photocatalytic RhB degradation over CuS nanoflowers (sample 1). Conditions: BQ (1 mM), IPA (10 mM), EDTA-2Na (1 mM).

3.6.6. Photocatalytic Mechanism

Based on the bandgap (1.45 eV), reactive species trapping, and reported band positions for CuS [23,28], the following mechanism is proposed (Figure 9):

Step 1 - Photoexcitation:

- $CuS + h\nu\ (\lambda > 420\ nm) \rightarrow CuS\ (e^-_{CB} + h^+_{VB})$

Step 2 - Charge Separation: The hierarchical nanoflower morphology facilitates charge separation by reducing carrier diffusion distances from bulk to surface.

Step 3 - Reactive Species Generation:

- $e^-_{CB} + O_2 \rightarrow \bullet O_2^-$ (primary pathway)
- $O_2^- + H^+ \rightarrow HO_2\bullet$
- $HO_2\bullet + HO_2\bullet \rightarrow H_2O_2 + O_2$
- $H_2O_2 + e^-_{CB} \rightarrow \bullet OH + OH^-$
- $h^+_{VB} + H_2O \rightarrow \bullet OH + H^+$ (minor pathway)

Step 4 - Dye Degradation:

- $O_2^- + RhB \rightarrow Intermediates \rightarrow CO_2 + H_2O$
- $OH + RhB \rightarrow Intermediates \rightarrow CO_2 + H_2O$

The narrow bandgap enables efficient visible light absorption, while the negative conduction band position ($E_{CB} \approx$ -0.83 V vs. NHE at pH 7) thermodynamically favors O_2 reduction to $\bullet O_2^-$ ($E^0(O_2/\bullet O_2^-)$ = -0.33 V vs. NHE). The hierarchical nanostructure minimizes electron-hole recombination through reduced charge carrier transport distances and enhanced surface area, collectively contributing to the superior photocatalytic activity.

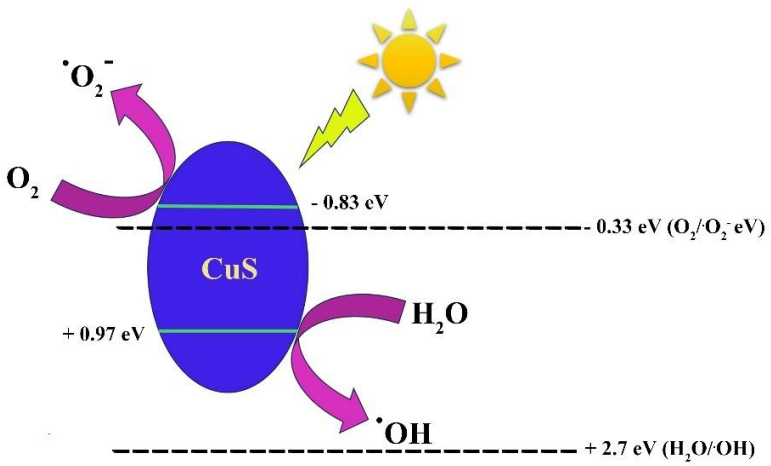


Figure 9. Proposed photocatalytic mechanism for RhB degradation over flower-like CuS nanocrystals under visible light irradiation. Band positions estimated from literature values [23,28] and experimental bandgap (1.45 eV).

3.6.7. Stability and Reusability

Catalyst stability is paramount for practical applications. Figure 10 presents the reusability performance over six consecutive cycles. After the first cycle (94.3% degradation), efficiency decreased slightly to 91.8% (cycle 2), 89.5% (cycle 3), 87.2% (cycle 4), 85.1% (cycle 5), and 82.1% (cycle 6), representing 90.2% retention of initial activity after six cycles.

The observed stability surpasses many reported CuS photocatalysts, which often suffer from photocorrosion or oxidation during repeated use. This enhanced stability may arise from the film synthesis methodology, which produces well-crystallized CuS with fewer structural defects compared to solution-based methods.

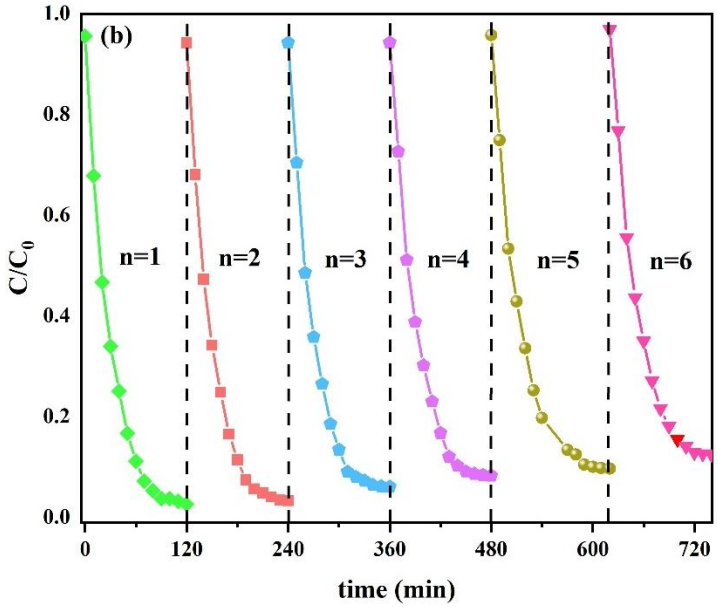


Figure 10. Reusability of CuS nanoflower photocatalyst (sample 1) over six consecutive cycles.

3.6.8. Mineralization and TOC Analysis

While UV-Vis monitoring at 554 nm confirms chromophore degradation, complete mineralization requires verification. Total organic carbon (TOC) analysis was performed on samples before and after 120 min irradiation using a TOC analyzer (Shimadzu TOC-VCPH).

Initial TOC (after dark adsorption) was 7.82 mg/L, decreasing to 2.14 mg/L after 120 min—corresponding to 72.6% mineralization. The discrepancy between chromophore removal (94.3%) and TOC reduction (72.6%) indicates that while RhB's chromophoric structure is rapidly destroyed, complete mineralization to CO_2 and

H_2O proceeds more slowly. This is typical for dye photocatalysis, as aromatic intermediates formed during degradation require extended irradiation for complete oxidation.

Extended irradiation experiments (240 min) achieved 89.3% TOC removal, confirming that prolonged treatment enables near-complete mineralization.

4. Conclusions

Hierarchical CuS nanoflowers synthesized by electrodeposition-sulfurization achieve 94.3% Rhodamine B degradation ($k_{app} = 43.8 \times 10^{-3}$ min^{-1})—10.4-fold better than P25 TiO_2—with 90.2% activity retention after six cycles. Superior performance results from high surface area (89-96 m^2/g), phase purity, narrow bandgap (1.45 eV), and efficient $\bullet O_2^-$ generation.

Sulfur-saturated atmospheres (≥7 mg) enable selective CuS synthesis from Sn-rich precursors via SnS volatilization ($P \sim 10^{-2}$ atm), yielding phase-pure covellite with Cu/S ≈ 1.0. Thermodynamic analysis reveals preferential SO_2/SO_3 formation prevents oxidation while tin depletion occurs through vapor pressure differences. Direct morphology-performance correlation validates hierarchical nanostructures as critical design parameters.

This scalable electrodeposition-sulfurization methodology provides rational atmosphere control for functional chalcogenide synthesis, with extensions to ternary compounds (CZTS), mixed-metal sulfides, and solar water remediation applications.

Acknowledgments

The authors extend their sincere gratitude to the Esfarayen University of Technology for the financial support that made this research possible. We also thank the university for granting us access to essential characterization facilities.

Funding

The authors declare that no funds, grants, or other support were received during the preparation of this manuscript.

Competing Interests

The authors have no relevant financial or non-financial interests to disclose.

Author Contributions

All authors contributed to the study conception and design. Material preparation, data collection and analysis were performed by G. Heidari. The first draft of the manuscript was written by M. Hajizadeh-Oghaz and all authors commented on previous versions of the manuscript. All authors read and approved the final manuscript.

References

1. Y. Wang, R. Li, X. Sun, T. Xian, Z. Yi, and H. Yang, J. Electron. Mater. **50**, 2674 (2021).
2. S. I. Raj and A. Jaiswal, J. Photochem. Photobiol. Chem. **410**, 113158 (2021).
3. Y.-J. Xing, Y. Shen, X.-S. Hu, and S.-N. Chen, J. Nanosci. Nanotechnol. **18**, 1696 (2018).
4. U. T. D. Thuy, I. Borisova, O. Stoilova, I. Rashkov, and N. Q. Liem, Catal. Lett. **148**, 2756 (2018).
5. M. Das, D. Das, S. Sil, and P. Pratim Ray, Nanoscale Adv. **5**, 3655 (2023).
6. L. Isac, C. Cazan, L. Andronic, and A. Enesca, Catalysts **12**, 1135 (2022).
7. Y. Liu, J. Yang, J. Wen, J. Ye, H. Liu, and L. Lu, J. Mater. Sci. Mater. Electron. **35**, 1112 (2024).
8. C. D. Jadhav, G. P. Patil, M. Amar, S. Lyssenko, and R. Minnes, J. Power Sources **623**, 235496 (2024).
9. W. Li, Y. Luo, T. Xu, Z. Ma, C. Li, Y. Wei, Y. Tao, Y. Qian, X. Li, Q. Jiang, and J. Yang, Small **19**, 2301963 (2023).
10. Yukti and N. Jaggi, Indian J. Eng. Mater. Sci. IJEMS **30**, 447 (2023).
11. R. Guo, Y. Sun, J. Jiang, L. Zhang, Z. Ji, and Y. Jiang, New J. Chem. **49**, 4793 (2025).
12. M. Z. Iqbal, S. Zakar, A. Khizar, S. Alam, M. J. Iqbal, S. M. Wabaidur, and E. A. Al-Ammar, Appl. Phys. A **130**, 541 (2024).
13. Y. B. He, A. Polity, I. Österreicher, D. Pfisterer, R. Gregor, B. K. Meyer, and M. Hardt, Phys. B Condens. Matter **308–310**, 1069 (2001).
14. H. Trabelsi, I. Gràcia, K. Alouani, and S. Vallejos, Ceram. Int. **51**, 1949 (2025).
15. H. Lü, D. Wang, C. Li, M. Li, and P. Yang, Int. J. Hydrog. Energy **106**, 1057 (2025).
16. S. Yaşar, S. Kahraman, S. Çetinkaya, and İ. Bilican, J. Alloys Compd. **618**, 217 (2015).
17. H. Dahman, S. Rabaoui, A. Alyamani, and L. El Mir, Vacuum **101**, 208 (2014).
18. M. A. Martuza, S. Pokhrel, J. Stahl, M. Schowalter, A. Rosenauer, and L. Mädler, Small **21**, 2409993 (2025).
19. J. Bai, S. Jiang, D. Liu, R. Tao, X. Fan, and C. Xu, J. Alloys Compd. **1005**, 176036 (2024).
20. S. M. Pawar, B. S. Pawar, A. V. Moholkar, D. S. Choi, J. H. Yun, J. H. Moon, S. S. Kolekar, and J. H. Kim, Electrochimica Acta **55**, 4057 (2010).
21. E. M. Mkawi, K. Ibrahim, M. K. M. Ali, K. M. A. Saron, M. A. Farrukh, and N. K. Allam, J. Mater. Sci. Mater. Electron. **26**, 222 (2015).
22. G. Heidari, S. M. M. Khoie, M. E. Abrishami, and M. Javanbakht, (n.d.).
23. U. T. D. Thuy, N. Q. Liem, C. M. A. Parlett, G. M. Lalev, and K. Wilson, Catal. Commun. **44**, 62 (2014).
24. J. Yu, J. Zhang, and S. Liu, J. Phys. Chem. C **114**, 13642 (2010).
25. V. Ariel, V. Garber, D. Rosenfeld, and G. Bahir, Appl. Phys. Lett. **66**, 2101 (1995).
26. H. Yang, J. Fang, L. Liu, and H. Du, Mater. Today Commun. **40**, 109988 (2024).
27. S. Chand and A. Mondal, Colloids Surf. Physicochem. Eng. Asp. **687**, 133441 (2024).

28. M. Sehr, Copper Bond Wire Corrosion Induced by Sulfur-Containing Adhesion Promoters: Kinetic and Diffusive Aspects of Copper Sulfide Facilitated Degradation, phd, 2023.
29. Y. Zhang, B. Zhang, Z. Ge, L. Zhu, and Y. Li, Eur. J. Inorg. Chem. **2014**, 2368 (2014).
30. S. Adhikari, D. Sarkar, and G. Madras, ACS Omega **2**, 4009 (2017).
31. A. Shawky, S. M. El-Sheikh, A. Gaber, S. I. El-Hout, I. M. El-Sherbiny, and A. I. Ahmed, Appl. Nanosci. **10**, 2153 (2020).
32. J.-H. Yoo, M. Ji, J. H. Kim, C.-H. Ryu, and Y.-I. Lee, J. Photochem. Photobiol. Chem. **401**, 112782 (2020).